Scanning Microscopy

Volume 1994
Number 8 *The Science of Biological Microanalysis*

Article 21

6-20-1994

Energy-Filtering Transmission Electron Microscopy as a Tool for Structural and Compositional Analysis of Isolated Ferritin Particles

A. L. D. Beckers
Erasmus University, The Netherlands

W. C. de Bruijn
Erasmus University, The Netherlands

J. F. Jongkind
Erasmus University, The Netherlands

M. I. Cleton-Soeteman
Erasmus University, The Netherlands

R. P. Apkarian
Emory University, Atlanta

Energy-Filtering Transmission Electron Microscopy as a Tool for Structural and Compositional Analysis of Isolated Ferritin Particles

Authors

A. L. D. Beckers, W. C. de Bruijn, J. F. Jongkind, M. I. Cleton-Soeteman, R. P. Apkarian, and E. S. Gelsema

Scanning Microscopy Supplement 8, 1994 (pages 261-275) 0892-953X/94$5.00+.25
Scanning Microscopy International, Chicago (AMF O'Hare), IL 60666 USA

ENERGY-FILTERING TRANSMISSION ELECTRON MICROSCOPY AS A TOOL FOR STRUCTURAL AND COMPOSITIONAL ANALYSIS OF ISOLATED FERRITIN PARTICLES

A.L.D Beckers[1], W.C. de Bruijn[2*], J.F. Jongkind[3], M.I. Cleton-Soeteman[4], R.P. Apkarian[5] and E.S. Gelsema[1]

[1] Department of Medical Informatics, [2] AEM-Unit, Department of Clinical Pathology,
[3] Department of Cell Biology and Genetics, [4] Department of Chemical Pathology, Erasmus University, Faculty of Medicine and Health Sciences, The Netherlands.
[5] Yerkes Regional Primate Centre, Emory Univ. Atlanta, Georgia, USA.

(Received for publication November 26, 1993, and in revised form June 20, 1994)

Abstract

Structural and compositional analysis of isolated horse-spleen ferritin particles was performed by energy filtering transmission electron microscopy (EFTEM). Ferritin particles were collected in ultrathin (2 nm thick) chromium films and analyzed without any additional stain by electron energy-loss spectroscopy (EELS) for iron and carbon and by electron-spectroscopic imaging (ESI) for carbon. The ultrastructure of the proteinaceous shell of the ferritin particle, as obtained by the carbon net-intensity electron spectroscopical and carbon concentration-distribution images, was qualitatively compared to the structure as acquired by a negative-staining procedure.

Quantitative analysis of the number of carbon atoms in the ferritin-shell proteins was carried out through an ESI-acquisition protocol and processing procedure with calibrated attenuation filters in the optical path to the TV camera. This procedure included images acquired with calibrated attenuation filters for the compensation of shading and the non-linear performance of the TV camera used in the analytical part of the procedure. A new "ESI-Spectra" program is proposed that allows element-related spectra to be generated at any place and with any frame size in a contrast-sensitive or other type of image present on the computer monitor screen.

Key Words: Energy-filtered transmission electron microscopy (EFTEM), electron spectroscopic image analysis, electron energy-loss spectral analysis, ferritin.

*Address for correspondence:
W.C. de Bruijn
AEM-Unit, Institute of Pathology, Ee 902,
Erasmus University of Rotterdam, PO Box 1738,
3000 DR Rotterdam, The Netherlands
Phone Number: 31+10+4087922
Fax Number: 31+10+4366660

Introduction

Ultrastructural observation of small isolated particles like ribosomes, viruses, lipoproteins has successfully been performed for several years with negative staining techniques [24]. Among these structures, ferritin particles have frequently been used as a test-object. With negative staining techniques the final resolution obtained was determined by the thickness and grain-size of the support film and of the staining material. The images formed are to some extent indirect, as it is the stain distribution that is imaged. The support film used in negative staining techniques has been formed either by metal evaporation [35] or by a chemical reaction [28]. Use of scanning transmission electron microscopical (STEM) analysis allows a more direct imaging from (isolated) biological structures [19, 27, 30, 37-39, 48]. Recently, Leapman *et al.* [38-39] have demonstrated STEM-imaging of frozen-dried biological materials.

Energy-filtering transmission electron microscopy (EFTEM) potentially allows observation by inelastically scattered electrons of isolated particles without any additional staining. In instruments with an in-column spectrometer, like the Zeiss EM 902, energy filtering has been used to acquire in addition to the element-related images, structure-sensitive information by zero-loss and $\Delta_{250\ eV}$ images. But image information in such $\Delta_{250\ eV}$ images is also to some extent indirect. Such images are acquired from a spectral region just before the carbon edge. Other elements present in the structure with edges below that of carbon appear as white, whereas the image contributions of carbon plus that of element edges beyond the carbon edge are absent and appear as black [44, 49].

Conversely, because element-related images can be acquired, proteinaceous structures can be imaged directly by their carbon content, which in biological particles may amount to about 50 atomic % of the total number of atoms. However, carbon-based structural EFTEM analysis in ultrathin sections has not been

successful for the following reasons:

(1) The carbon in the proteinaceous structures is surrounded by or even infiltrated with a carbon-rich embedding medium, which annihilates carbon contrast.

(2) Routinely obtained 50 nm thin sections might be considered too thick to render sufficient contrast regarding the intensity reduction by energy-filtering. This has resulted in the use of unsupported ultrathin (as thin as possible) sections.

(3) Superimposition of objects will disturb both the spatial resolution in general and may hamper determination of element concentrations. In an attempt to analyze ferritin-particle clusters in liver parenchyma cells, four particles with a mean protein particle diameter of 12 nm might be present on top of each other in the 50 nm layer in ultrathin sections. For that reason, direct ferritin-carbon imaging preferably should be performed in a model system with isolated single particles in a thin non-carbonaceous environment, like thin metal films [42].

Recently, acquisition protocols and image-processing procedures have been proposed for combined structural and compositional analysis of elements in ultrathin biological sections [4, 13-15]. These ESI analyses have been applied to determine the iron concentration in large iron-containing particles, the liver siderosomes and to estimate the calcium content of oxalate crystals.

In the acquisition protocol, several energy-filtered images have to be acquired in sequence, including zero-loss plus low-loss images acquired with the use of attenuation filters, both in the unknown and in a co-embedded Bio-standard. The duration of the total acquisition period of that protocol is $\pm$ 400 seconds. In this respect, questions have been raised about superimposition, instrumental and specimen stability in relation to the spatial resolution and precision, which are of interest to be elucidated. To study these aspects also a single-particle model system had to be adopted.

The technique used (which originally has been proposed for negative staining of isolated particles by Horne and Pasquali-Ronchetti in 1974 [26]) enabled us to obtain the requested certainty that one is dealing with a single layer of neatly arranged particles, embedded in a thin film. Recently a technique to produce extremely thin metal (chromium) films became available [2] which permitted us to fulfil all conditions mentioned and to visualize and possibly to quantify the carbon contents of isolated proteinaceous structures in ferritin particles.

In principle, such a model system also lets the number of atoms as determined -*in situ*- by EFTEM, either for the iron in the 6 nm diameter core or the carbon in the proteinaceous shell to be compared to the values determined by bulk chemical analytical techniques from the same solution [8-10, 41]. We will concentrate on the carbon visualization by ESI of energy-filtered inelastic-scattered electrons and on a method to estimate its carbon contents.

The aim of our investigation is twofold:

(1) To explore the electron spectroscopic imaging characteristics of carbon from the proteinaceous mantle of the ferritin,

(2) To test the value of the EFTEM acquisition protocol and element analysis procedure proposed previously [4, 13-15] to obtain quantitative information about carbon and to investigate aspects of stability, contrast, noise, mass-loss and spatial reproducibility.

Materials and Methods

Ferritin particles were obtained from a commercially available stock solution of horse spleen ferritin (Sigma, Bornum, Belgium). Samples of this solution were diluted with double distilled water to an optical density of 0.2 at 595 nm (= 0.2 mg/ml). The Horne/-Pasquali-Ronchetti technique was slightly adapted: we used a lower ammonium molybdate concentration and no ethylene glycol. Prior to use, ammonium molybdate tetrahydrate (Fluka, Bornum, Belgium) was added to droplets of the ferritin solution to a final concentration of about 1 wt %. Drops of this mixture were spread on freshly cleaved mica sheets (Agar Aids, Stansted, U.K.) by a glass rod. After an initial drying at air, the sheets were evaporated -*in vacuo*- with a carbon film (Bio-Rad, E9000-Coater, Veenendaal, The Netherlands). Similar air-dried mica sheets were covered by magnetron-Argon sputter coating with a very pure chromium film, in a Denton DV-602 turbo-equipped sputter deposition system. The integral water-cooled cathode (DSM-300A) was operated at 50 mA for 60 s at a cathode/target distance of 5 cm. The deposition thickness was measured by a quartz crystal thickness monitor. The films were floated-off on water and collected on 500 mesh copper grids without film. Chromium, which has a grain size of about 0.2 nm, appears even at 0.5 nm thickness as continuous in TEM instruments with 200 kV acceleration voltage. Such tightly packed chromium films oxidize only at the surface when in contact with air. This converts the film partially into a chromium oxide film. The films on the grids were observed without any additional staining. An assumed cross-section of such films is shown in Figure 1. An aqueous uranyl acetate solution (1 wt%) was used for negative staining.

The analytical instrument was a Zeiss EM 902 (Zeiss, Oberkochen Germany) with an in-column spectrometer of the prism/mirror/prism type according to Castaing/Henry/Ottensmeyer (Figure 2). Instrumental details are given elsewhere [12-15, 49-52].

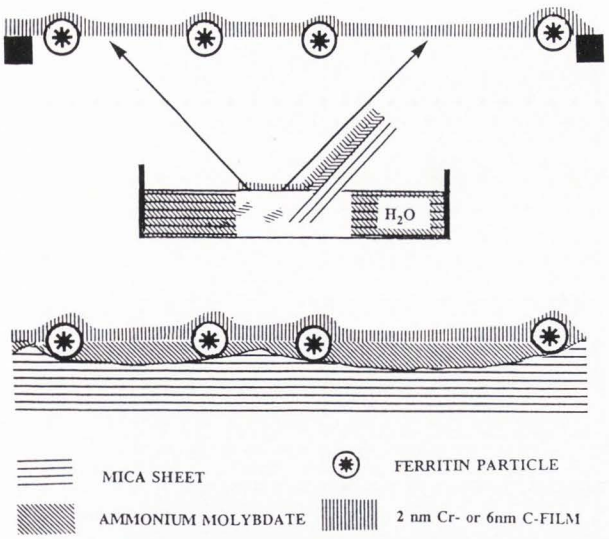

Figure 1: Schematic view of the preparation procedure to obtain the isolated ferritin particles attached to the thin carbon or chromium oxide films.

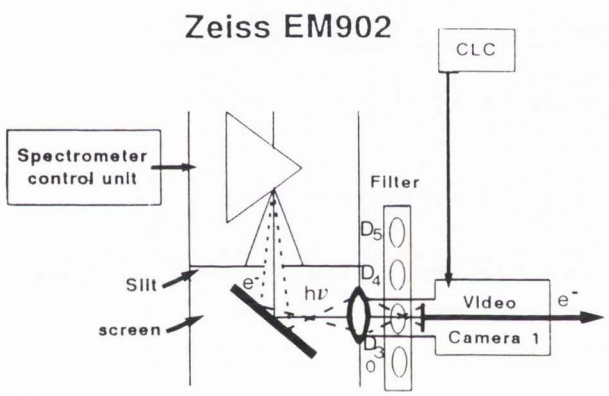

Figure 2: Schematic view of the Zeiss EM 902 image chain plus some of its peripheral instruments. C.L.C. = camera light controller.

Serial electron energy-loss spectral (EELS) analysis was performed on a varying number of ferritin particles at 85,000 X magnification [analyzed area: 23,235 nm^2, acceleration voltage 80 kV, slit width 1-2 eV, objective-lens aperture (β=) 17 mrad]. Spectrum processing was performed by a Simplex fitting procedure [12, 51] with the use of a pre-edge fitting region (Γ) = post-edge extrapolation region (Δ): 100 eV. Analysis was performed at the carbon (C_K) edge at 284 eV and the iron ($L_{2,3}$) edge at 708 eV.

Electron spectroscopic image analysis (ESI) was performed at 50,000 X instrument magnification (pixel area: 2.25 nm^2). From the unstained or with uranyl acetate negatively stained specimens, energy-filtered images were acquired at zero-loss, excluding most inelastic-scattered electrons and around the carbon edge at 284 eV. The acquisition protocol included several images around the carbon edge plus images taken at the zero- and low-loss region with a (D = 4.0 or 3.0) attenuation filter installed, all acquired in one run. The slit width was 20 eV, the width of the Γ region 100 eV (five images) and the width of the Δ region 60 eV (three images). Several additional optical-filtered images were acquired to correct for offset and for the non-linearity of the camera. It has been shown before that the multiplicative shading is removed once the concentration proportional (R*)-image is obtained through division of the carbon net-intensity ($I_K(C)$ - I_b) image by the (summed) zero-loss and low-loss (I_T) images [4, 15].

The images were partially processed -on line- in an IBAS 2000 (Zeiss/Kontron, Oberkochen, Germany) and -off line- in a Hewlett-Packard 9000-735 work station (Hewlett Packard, USA) assuming a power-law relation for the continuum, by the algorithm recently proposed by Beckers *et al.* [3]. The first image acquired in the series was re-acquired at the end of the acquisition run, to allow the evaluation of drift, mass-loss and stability. The first pre-edge image, with an energy-loss of 184 eV was used as the contrast-sensitive image. In this image the ferritin iron cores were located using a top-hat filter [40], skeletonized to one pixel and subsequently dilated circularly to acquire a true area of 13 nm diameter to enclose the entire proteinaceous shell of the ferritin particle. The true summed area of the identified ferritin particles was determined for a central part of the original 512^2 images, measuring 256^2 pixels in toto. Pixel sizes were calibrated using a grating replica as described previously [49].

Element-concentration are simultaneously computed. Spectra can interactively be reconstructed (ESI-spectra) from the sequence of spectral images within any area of interest in the image and from areas with variable sizes.

The final images were recorded by a Polaroid freeze frame on Kodak black and white film, or directly from the monitor or as photostatic hard copies.

The wet-chemical analysis for iron was performed according to Bradford [7] from the same stock solution. Similarly, the wet chemical analysis for total protein was performed by an adaptation of the method of Harris [23]. For details see van Gelder *et al.* [57].

Results

Figure 3a, shows an analog contrast-sensitive micrograph acquired under zero-loss conditions. The presence of the ferritin particles is demonstrated by the iron cores in ferritin-particle lakes surrounded by bare chromium film. The fine grain of chromium film can be seen in these areas not occupied by ferritin particles. In

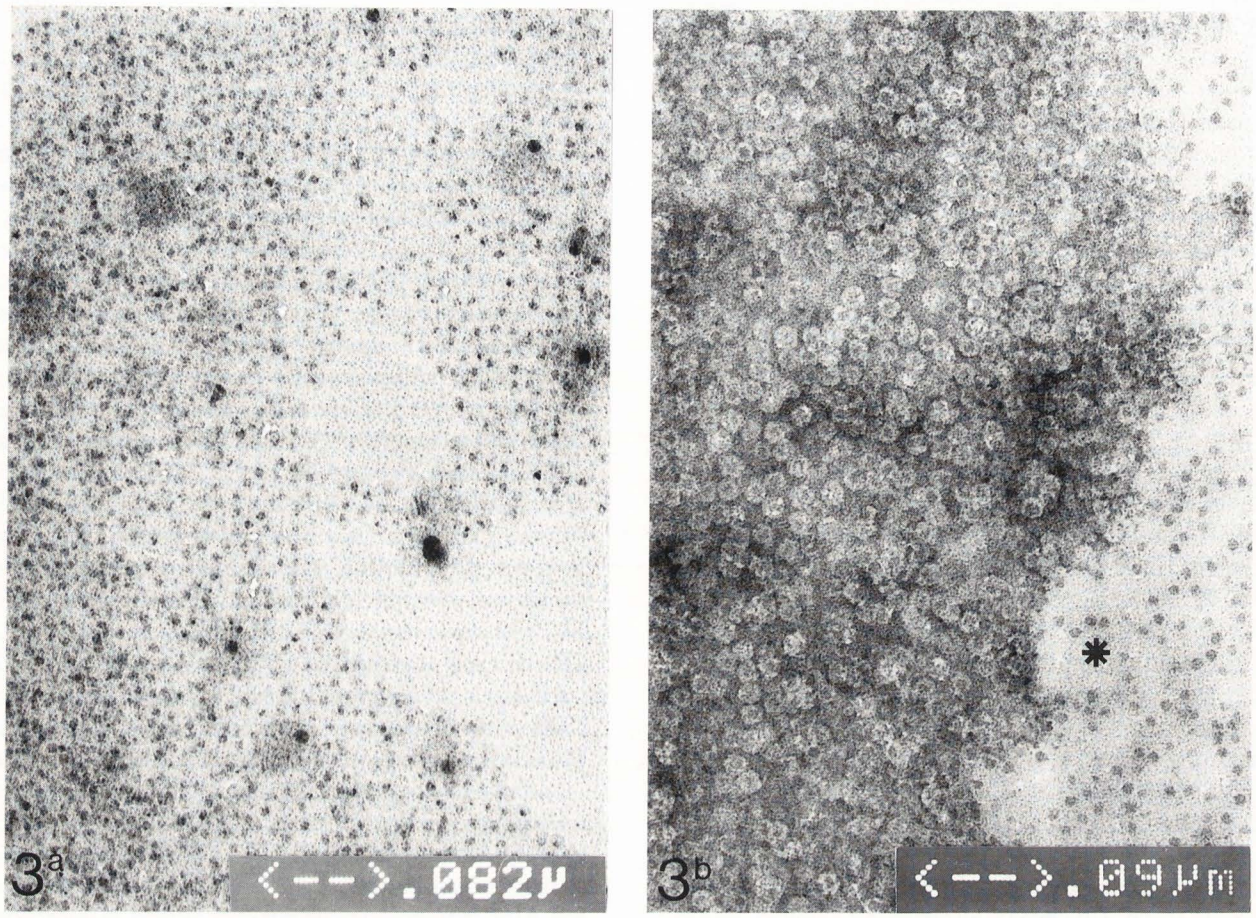

Figure 3: Analogue image of the ferritin particles in a thin chromium oxide film (a) zero-loss image unstained, (b) zero-loss image of negatively stained ferritin in a carbon film. Note the partial failure of the negative staining (*).

Figure 3b, the analog contrast-sensitive zero-loss image of a negatively stained specimen displays the presence of the proteinaceous mantle around the central core. At some places (*) the uranyl acetate negative staining fails to stain.

In Figure 4, a serial EEL-spectrum is shown from ferritin particles in lakes in the chromium oxide film, showing all edges in one.

In Figures 5-6, carbon (5) and iron (6) edges are shown: (a) as acquired (b) following Simplex continuum fitting and (c) after continuum subtraction. Clearly the presence of carbon in the analyzed ferritin-particle area is shown. The subtraction of the continuum under the iron edge is hampered by the presence of the chromium edge at 574 eV and the oxygen at 532 eV in the pre-edge region and the possible presence of the L_1 edge at about 690 eV. For this reason we refrained from quantitative iron measurements in the ferritin particles in the chromium films. The net-carbon-edge is quite prominent with an undisturbed pre-edge region, although a minor influence from the tail of the chromium $M_{2,3}$ edge beyond 40 eV might be present.

Figure 7a shows the digital zero-loss image, in which iron-cores are visible and the proteinaceous material is slightly different in contrast from the free chromium oxide film. In Figure 7b, in an area neighbouring that of Figure 7a, the carbon net-intensity image ($I_K(C) - I_b$) is shown. The presence of carbon in the proteinaceous shells is seen in white. In 7c, the concentration proportional R^*_C image $[(I_K(C) - I_b)/I_T]$ from the same area is shown. In Figure 7b, the position of the iron core can be observed through the carbon in the proteinaceous shells (by the relative absence of carbon) in black. The contrast between the mantle and the core in the R^*_C image in 7c is reduced, after correction for the high local core-mass density. The carbon contents of the proteinaceous shell is visible in projections of substructures (Figure 7c inset). At the periphery of some ferritin lakes a fine flocculent carbonaceous material is present, which remained unobserved in the negatively stained specimen. The nature of it has to be established.

In Figure 8a, the digital carbon pre-edge image is

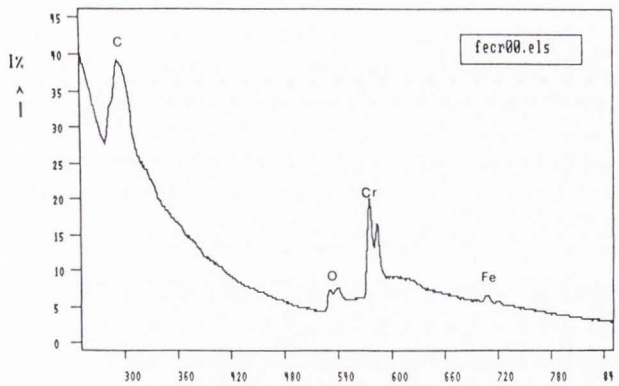

Figure 4: Total serially acquired spectrum of an analyzed area in a ferritin-particle lake, showing the carbon, and iron edges and the film-related chromium and oxygen edges.

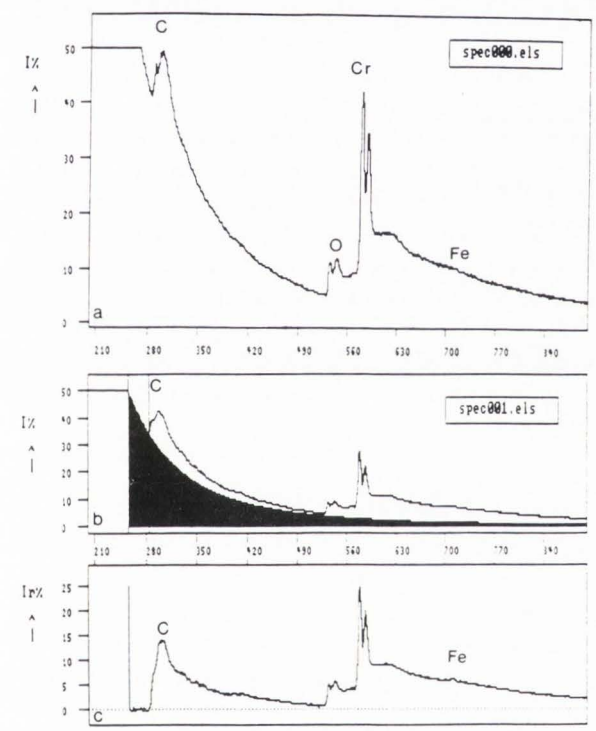

Figure 5: Carbon-related spectrum detail of the same analyzed area. (a) total spectrum, (b) Simplex fitting procedure, (c) continuum-subtracted spectrum.

shown with the discriminated ferritin particles following top-hat filtering and skeletonization to one pixel. In Figure 8b, the areas with a 13 nm diameter around these centres are shown by discrete circles.

Calculation of the amount of carbon in ferritin particles

According to the theory the number of carbon atoms

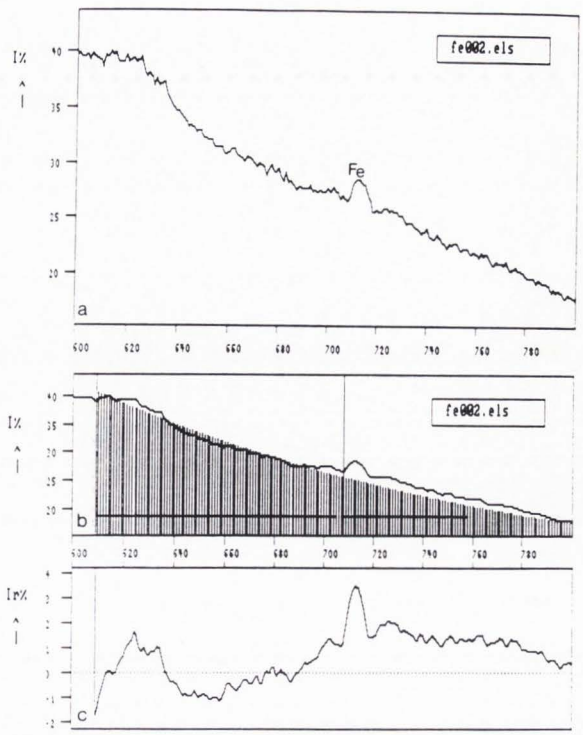

Figure 6: Iron-related spectrum detail of the same analyzed area. (a) total spectrum, (b) Simplex fitting procedure, (c) continuum-subtracted spectrum.

N_C in an analyzed area is given by:

$$N_C = \frac{netI_K(C)(\beta,\Delta)}{I_T(\beta,\Delta).\sigma_C(\beta,\Delta)} \qquad (1)$$

in which I_T represents the total intensity image acquired in the zero-loss plus low-loss part of the spectrum, σ_C the partial cross-section for carbon and β and Δ are instrumental parameters mentioned in Materials and Methods. Defining the concentration proportional ratio image R^*_C = net $I_K(C)/I_T$, this image is proportional to the number of carbon atoms in the analyzed area, accordingly:

$$N_C = \frac{R^*_C(\beta,\Delta)}{\sigma_C(\beta,\Delta)} \qquad (2)$$

Once a reliable figure for σ_C can be obtained and the number of ferritin particles per frame area is established the mean N_C can be calculated.

Recently, Hofer [25] compared σ_C values from the Hartree-Slater model, the hydrogen model and the experimental results from various authors (for an accelerating voltage of 120 kV, β = 5,9 mrad and Δ = 100 eV) and found values between $4.1\text{-}4.8\text{x}10^{-21}$

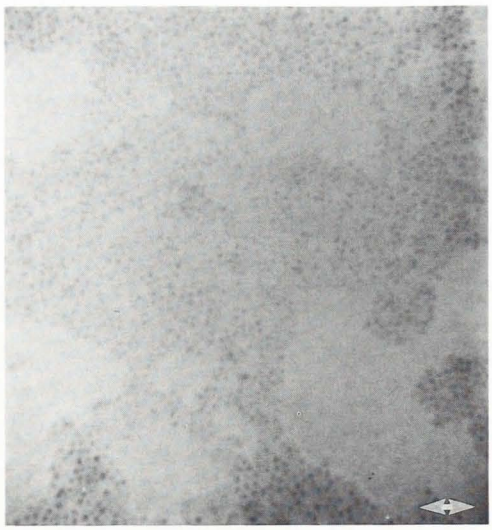

7a

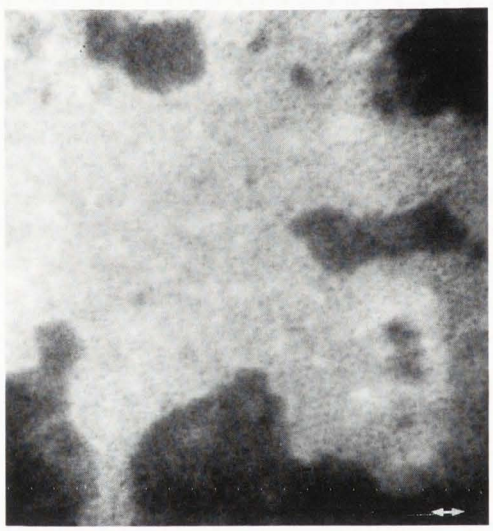

7b

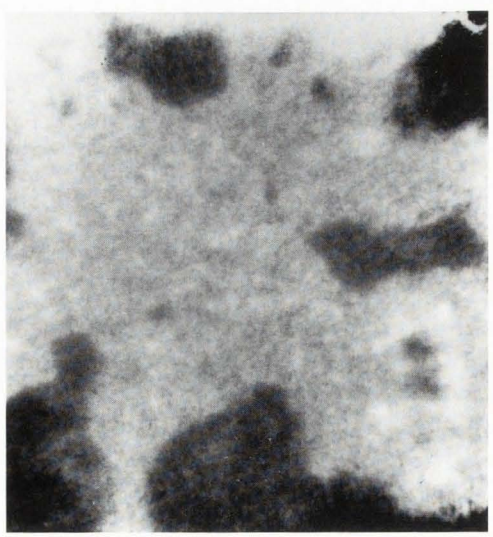

7c

Figure 7: (a) Digital zero-loss image of a ferritin lake in the chromium oxide film (Bar=50 nm). (b) Carbon-related net-intensity image of a ferritin lake. (c). Carbon-concentration distribution (R^*_C) image of the same area as shown in (b). Inset in 7c is a computer screen magnification of a small area of Figure 7b. Arrows point to globular sub-structures around the central core. (Bar in 7b = 25 nm, pertains to image c).

Table 1. Analyzed areas in EELS and ESI mode

Magnification	Analyzed area in EELS	Pixel area (512^2) in ESI
50,000 x	196,350 nm^2	2.25 nm^2
85,000 x	23,235 nm^2	< 1 nm^2

cm^2/atom. Our images are acquired at 80 kV, β = 17 mrad, and Δ = 60 eV. We used the SIGMAK$_2$ program as proposed by Egerton [17], from which a σ_C = 7.3×10^{-21} cm^2/atom, was calculated, to work with. This value seems reasonably correct because for an acceleration voltage of 120 kV, β = 5.9 mrad and Δ = 100 eV a σ_C value of 4.8×10^{-21} cm^2/atom is calculated. Our calculations were performed for the centrally located 256^2 pixel frame. For the calculation of the carbon content two approaches can be chosen:

(a) to calculate the total carbon content of a selected analyzed frame, or

(b) to calculate the carbon content per ferritin particle.

In the former case, the concentration distribution image R^*_C of a 256^2 frame is segmented based upon a signal to noise ratio (SNR) SNR-net $I_K(C)$ = 2.25 σ-value (not shown). In the latter case, the first image taken in the pre-edge zone (at 184 eV) is used as a contrast-sensitive image to discriminate the ferritin particles by top-hat filtering as described. In the central 256^2 area 312 ferritin particles were discriminated, about 40 pixels/particle each (Figures 8a and b). The mean SNR-net $I_K(C)$ per pixel is = 3.03 and consequently the SNR-net $I_K(C)$ per ferritin particle is 20.3. Based upon the σ_C value of 23.0×10^{-21} cm^2/atom, the total amount of carbon detected in a 256^2 pixel area is: 9.7×10^6 atoms. The number of carbon atoms calculated from the 312 segmented particles is 16,874 atoms per ferritin particle. Analysis of the negatively stained ferritin particles revealed a mean core diameter around 6.0 nm and a mantle diameter of about 12 nm (Figures 3a,b).

Spectral analysis from selected areas (ESI-spectra)

The analytical procedures in STEM instruments as compared to EFTEM instruments like the Zeiss EM902

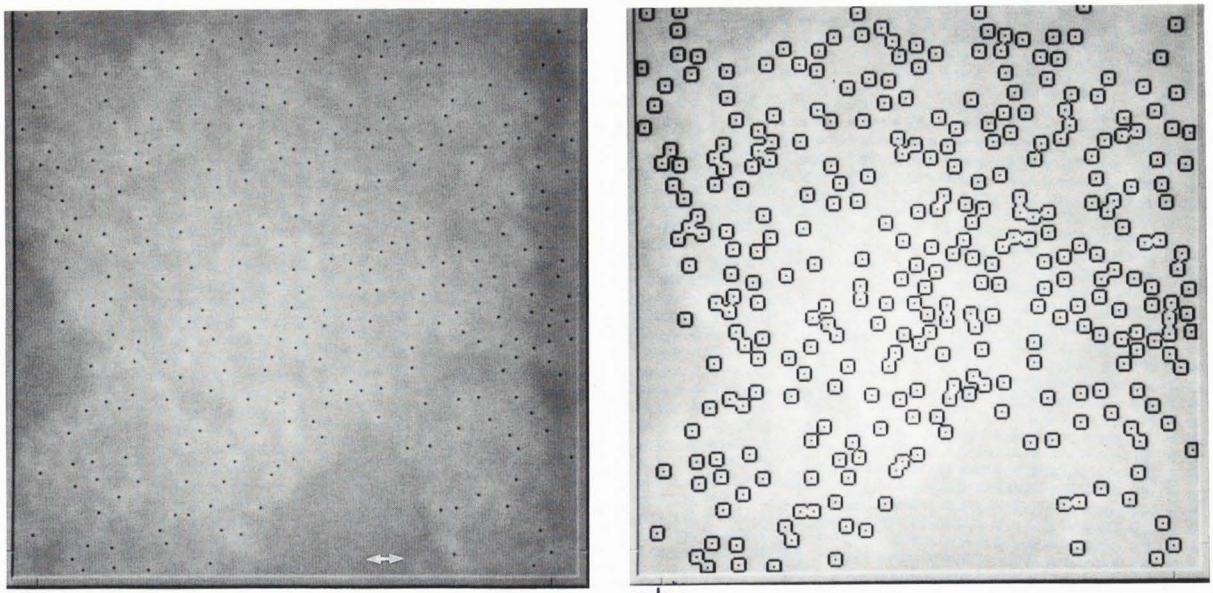

8a 8b

Figure 8: (a) Segmentation of the ferritin cores by the top-hat filter, skeletonization to one pixel (b). Expanding the area around the detected core centres to a true area of 13 nm in diameter.

have in common, that the acquired chemical information can be related to structural information. In both type of instruments for that purpose two strategies are available by: (a) obtaining spectral information or (b) obtaining pixel information from a series of spectroscopic images. In both cases, in the specimen:

(1) The chemical spectral information from an analyzed area can be related to an image with structural information from that area (= point analysis).

(2) Element related images are pixel-wise correlated with a serially or sequentially acquired contrast-sensitive image (image analysis).

In Figure 9a and 9b, the similarity of the point-analysis approach between the types of instruments is shown (o ↔ spectrum). The differences between the two types of analysis is found in the element-related image acquisition [13, 27]. In short: in EFTEM, spectral images are acquired with all pixels in parallel but in spectral sense (eV direction) serially (Figure 9a). In STEM, the spectral information is acquired in parallel (Figure 9b :eV) from (x-y) positions acquired serially (o o o o).

The spot size in some STEM instruments with a field-emission source can be reduced to 1 nm. The duration of the total acquisition is determined by the dwell time per point and the number of points needed to cover the image. The size of analyzed area in EFTEM is connected with the instrumental magnification. For two acquisition modes in the EM 902 these values are shown in Table 1. The duration of the total acquisition is determined by the number of spectral images and the number of integrations per image. Although with increasing magnification the analyzed area in the spectral EELS mode is further reduced, and alternatives in the image mode are present, the values in Table 1, indicate an analyzed-area restriction for EELS when very small particles have to be analyzed at low magnification.

To alleviate this analyzed-area problem, a computer program (called ESI-spectra) is developed to reconstruct spectra from a series of electron spectroscopic images acquired from a certain analyzed area, containing several small particles. The x-y freedom and the variable spot size (present in the scanning mode of STEM type of instruments) are in this program now replaced by the positioning of the mouse of the computer and keys for scaling. Using one image from the multi-spectral set for structural reference (zero-loss, $\Delta_{250\ eV}$ or element-related images) pixels, areas or objects can be randomly addressed for analysis to generate reconstructed spectra from a particular element acquired before. Any frame size and in principle any shape can be selected for spectrum reconstruction. The pixels in the selected area can be summed, so spectra with an improved SNR can be obtained. The reconstructed integral spectrum shows the element-related spectrum around the edge, the power-law background is fitted on the fly and at the same time the element-concentration related values are given in the corner of the screen. The reconstructed spectra can be processed for the detection of minor edges according to algorithms available for parallel or serial spectra.

This illustrative technique is used to reconstruct

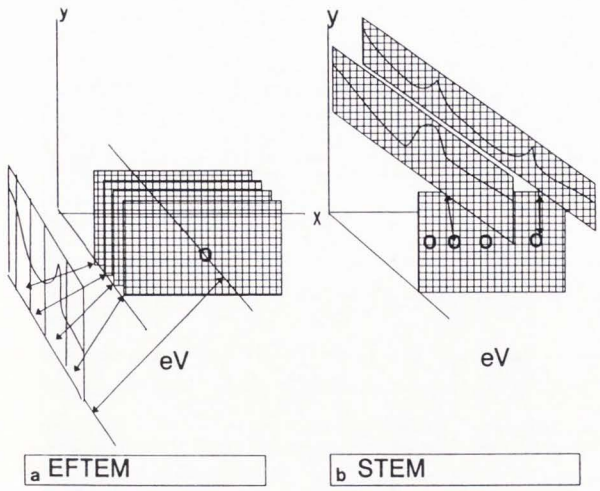

Figure 9: Schematic view of serial EFTEM analysis by ESI (a), as compared to the image acquisition by a STEM instrument (b).

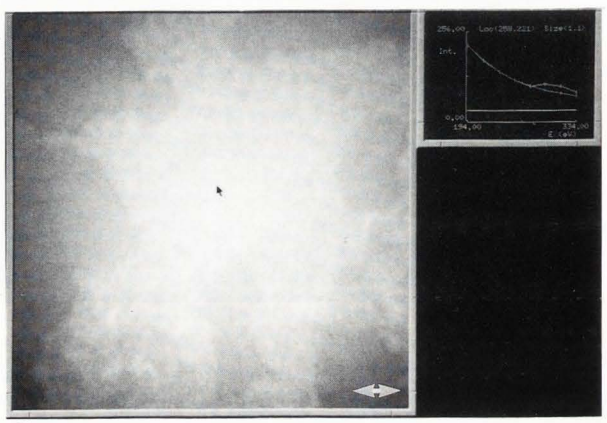
10 a

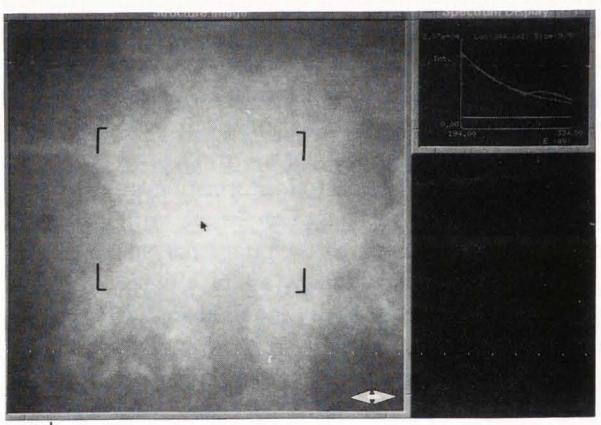
10 b

Figure 10: Impressions from the computer screen. (a) Carbon-spectrum reconstruction by the ESI-Spectra program from a 1x1 pixel area in a ferritin-covered site. (b) Similar spectrum from an area expanded to 9x9 pixels (arrow) from a ferritin particle containing site. (c) Integrated carbon spectrum of the 312 top-hat detected particles. In Figure 10b, the area where the discriminated ferritin particles are located shown in Figure 8a and 8b is framed. The bar represents 50 nm.

carbon spectra in a single pixel, which is very noisy and from a frame area covering about one whole ferritin particle, having a greatly improved SNR. In Figure 10a, the reconstructed spectrum around the carbon edge is shown acquired from an 1x1 pixel frame in a ferritin containing lake. In Figure 10b, the reconstructed spectrum around the carbon edge is shown from a 9x9 pixel frame located over a carbon-containing area in the previously described 256^2 central area of the image. The area of this frame might be considered to contain a single ferritin particle. The reconstructed spectrum from a 9x9 frame located over an area assumed to contain only the chromium film resulted in a spectrum without any carbon present. At places, small fragments with a low carbon signal/concentration are found. In contrast to this interactive technique, a whole field of these particles can be detected using the top-hat transformation of one of the pre-carbon edge images (Figure 8). In Figure 10c, the integrated carbon spectrum is shown from the 312 by top-hat filtering segmented ferritin particles.

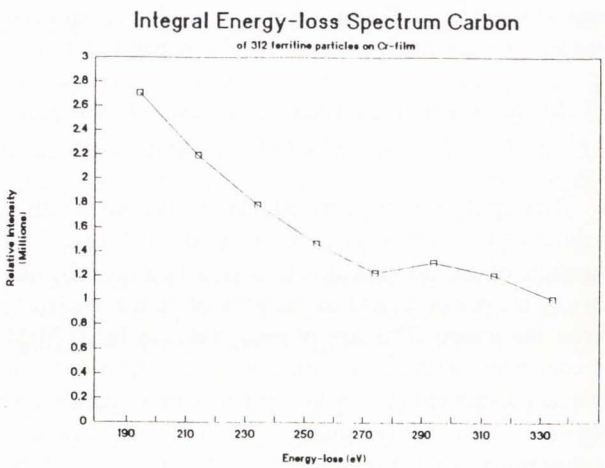

Validity checks

With the acquired (additional) images a series of

validity checks of the data has been performed to recognise specimen drift and radiation damage, and to learn to what extent the obtained data are suitable for the analytical questions to be answered.

Specimen drift and mass-loss during the acquisition of the series of images is monitored by re-acquisition of the first spectral image of the series at the end. Subtraction of the two images demonstrated the presence of possible specimen drift, which appears as a number of structures in the difference image. This specimen drift can be compensated. In this series only a minor specimen drift was present which is not corrected.

The chromium film with ferritin particles appears to be rather stable with respect to radiation damage over the acquisition period, which is obtained from the comparison of the grey-value image sums of the double acquired images. Although, the electron intensity was the maximum to be obtained from the tungsten hairpin filament a fraction of the carbon remains stable.

Four out of five pre-edge images are used to calculate the continuum of the fifth pre-edge image to demonstrate the absence of any detectable element. Since only pre-edge images without element information are used, the estimated continuum image should be equal to the fifth pre-edge image itself, apart from noise differences. Such a check is similar to the use of ghost images proposed by Bonnet *et al.* [5-6]. The last pre-edge image and the ghost image were virtually identical. As a result of these checks the image set is considered to contain sufficiently reliable information to answer questions about carbon imaging and quantification. For larger magnifications under almost focused beam conditions, the instrumental primary-beam drift might cause a time-dependent shading factor not modelled by the applied correction procedures and consequently rendering unusable data sets.

Discussion

Isolated ferritin particles have been used for years to demonstrate the analytical and instrumental potentials, both for transmission or scanning electron microscopy or for analysis by energy-dispersive X-ray spectroscopic (EDXS) and EELS microanalysis, [1, 8-11, 41, 48].

In our previous investigations about ESI analysis a protocol has been proposed about the use of attenuation filters. The aim was to acquire the edge intensity images and the zero- and low-loss images with the same camera settings and finally to obtain mass-corrected element distribution images [4, 12-15]. In these investigations, iron has successfully been shown to be present in concentration-distribution images of large siderosomes in liver cells from patients with an established haemochromatosis. An iron-positive area in the cytoplasmic periphery of these siderosomes was observed in which it was assumed that cytosolic ferritin could be present there. Because the spatial resolution in that area did not allow the recognition of discrete iron cores, we could not exclude the possibility of super imposition of several ferritin particles within one (50 nm) thickness of that section.

Hence, questions about the localization sharpness of the iron-concentration images with respect to the contrast-sensitive images, could be answered positively for the large siderosomes, but could not be answered with certainty for smaller ferritin cores. For that reason we returned to the Horne/Pasquali-Ronchetti technique. We used the isolated ferritin particles as a model to alleviate the chance that particles are superimposed by having them attached into a film-substrate of known thickness and composition. This allowed us in addition to use an element other then carbon for the support film and to investigate the possible use of carbon as a protein-imaging element in EFTEM.

The properties of the relatively unknown Horne-Pasquali technique (Figure 1) will be discussed briefly. The crystalline surface structure of cleaved mica sheets is used to (deliberately) create a local concentration in a pseudo array, although isolated single particles can be found. Pseudo arrays are a prerequisite for structural reconstruction by (optical) diffraction but single particle areas might be preferred. The presence of fine-grain ammonium molybdate in the suspension supports the particles when spread over the solid mica surface, preventing them to collapse during air drying and providing a water soluble interface for floating-off the film. Its concentration was reduced, because the risk of modification of the particle's architecture was accepted. The molybdate is considered to be removed from the specimen as no edge was observed ($M_{4,5}$ = 227 eV). The thin chromium films used were 1 and 2 nm thick, the former disintegrated while floating-off, the latter produced rather small flakes, that could be picked-up by grids without films. For these reasons we refrained from covering isolated chromium film with droplets of ferritin particles. The grain size of the chromium film (o,3 nm) is such that imaging of particles with a diameter of 6-12 nm is feasible. The embracing contact of the small particles by the film is again assumed to prevent architectural damage and is considered to minimise the effect of radiation damage, but there is no guarantee that the film has an equi-atomic thickness all over the place. Selection of a different film-element is feasible but several aspects need attention among which its Z-number, ionization energies and grain size in relation to the particle size to be imaged. The contrast between the film

and the carbonaceous material was, while designing the experiment, considered to be adequate for imaging and acceptable for the quantitative aim of this study. However, the aspects of the unstained structures seen (Figure 7c, inset) are somewhat different from those acquired by negative staining (Figure 3b), and justify further investigation. The presence of apo-ferritin-mantle fragments between the undamaged particles was anticipated. The fine granular proteinaceous material considered to remain partially unobserved (Figure 3b) in the negative stained samples due to coverage by the stain also hampers observation of structural carbon details in unstained ferritin lakes (Figure 7c inset).

The global segmentation procedure, satisfactorily applied before for the large siderosomes in the iron net-intensity image [4, 52] has recently been considered to be inadequate. This procedure has been abandoned and is replaced by a local segmentation procedure proposed by Beckers *et al.* [4]. A similar type of acquisition protocol and calculation procedure is applied to the ferritin model and carbon concentration-distribution images (R^*_C) could be generated.

Iron and carbon are detected by EELS analysis from rather large quantities of ferritin particles per analyzed area. Due to the rather neat arrangement of the ferritin particles within the lakes, the number of iron cores per unit analyzed area does not change drastically. However, it is noticed, that the chromium edge in front of the iron edge seriously influenced the determination of the iron concentration. For that reason we restricted the quantitative image analysis to the carbon, presuming that when it could be demonstrated that carbon could be quantified by this method in ferritin particles, iron quantification could also be achieved.

A comparison of the (analogue and digital) images acquired under zero-loss conditions from the negatively stained (Figure 3b) with the unstained ferritin particles (Figures 3a and 7a) does not attribute new aspects. In the negatively stained image the particle is dominated by the electron dense central iron core and the proteinaceous mantles look like flat rings around it. The ferritin particles in the carbon net-intensity and the concentration proportional R^*_C images (Figures 7b,c) look slightly more three dimensional, because the carbon of the mantle material is seen located over the core. Whereas the impression of the presence of a central core is not lost. However, the demarkation of the mantle at the outside of particles is less prominent, partially due to the rather close arrangement of the particles in the lakes in this specimen. In spite of the applied air drying, our results favour the idea that some improvement has been achieved by carbon imaging, where small proteinaceous fragments have been imaged, which remained unnoticed in the negatively stained specimen, but the pixel size and the final grain size of the film limits the spatial resolution for imaging.

The acquisition of the series of images and the applied image processing procedure in combination with the validity checks allows the carbon in these particles to be observed and to be measured. However, there is a trade off with respect to the number of electrons that are available for image formation both by increasing magnification and by imaging elements with edges at increasing distance from the zero-loss position in the spectrum.

With respect to the total intensity reduction, inevitably related to the energy-filtering, the reduction around the carbon edge might be sufficiently moderate to allow adequate imaging with an acceptable noise level from such particles 12 nm in diameter. It has to be shown, whether the intensity reduction at 708 eV, around the iron edge, will allow us to obtain quantitative results from the 6 nm cores.

Noise reduction can improve the quality of the acquired images by:

(a) Prolonged duration of the acquisition or the number of image integrations,

(b) Spatial filtering techniques, and

(c) Correspondence analysis.

The "ESI-spectra" computer program, is an attempt to solve in a more general way an EM902-related problem, partially tackled by Image-EELS [29, 36]. To get a sufficient number of electrons for image formation, three important decisions are to be taken in addition to the aspect mentioned under (a):

(1) The channel width has to be increased. Hence, the spectral resolution, as compared to the serial EELS is reduced (>5 eV versus <2 eV per channel). To maintain a certain signal level a trade-off has to be made between spectral resolution and spatial resolution. For EFTEM with the EM 902, this trade-off is made in the advantage of spatial resolution using a fixed 512^2 image raster.

(2) The summation of pixel values per channel over a selected area. This is similar to uniform low-pass image filtering using the selected area shape. Some results on low-pass filtering and smoothing techniques are given by Bonnet *et al.* [6], and Quintana and Bonnet [43] for STEM instruments.

(3) Continuum correction procedure. When used for (semi) quantitative analysis, the question may be raised whether to perform the continuum correction on the basis of the summed spectra as is done in case of "Image-EELS", or to perform it pixel by pixel and adding the net-intensity results afterwards or even after dividing by the zero- and low-loss contributions.

Especially when, as in our case, mass-thickness correction is performed by division of the zero- and low loss images, the summed approach gives generally biassed results. As an example, for two image locations with "a" and "c" being their net-intensity values and "b" and "d" their corresponding zero- and low loss values, the result obtained from summed spectra is (a+c)/(b+d). This is not equal to the result from a pixel-wise calculation: a/b + c/d, which is the desired result. We therefore adhere to the opinion that for qualitative results our described "ESI-spectra" procedure is useful and illustrative, but for quantitative purposes all relevant computations should preferably be performed pixel by pixel.

The quantitative procedure applied to the series of ESI images around the carbon edge heavily rests on the morphometric values from ferritin particles (a 6 nm diameter core plus 12 nm diameter mantle) which are generally accepted to be correct. As can be deduced from Figures 3a and 3b, these values are present in our ferritin samples.

Previously, the mean iron core diameter measured by the IBAS from Epon-embedded human ferritin and human ferritin spread on carbon films was between 6.0 - 6.9 nm $\pm$ 0.5-1 nm (n = 2,400 cores, 54 pixels/core) [45-47, 50].

Wet-chemical determination of carbon per ferritin particle remains a problem and reliable values are not available at this moment. A confusing aspect is the ratio between the number of ferritin particles discriminated by the top-hat filter procedure and the total amount of carbon measured in the area. The discrepancy lies in the observation that the calculated total amount of carbon atoms would represent 1,33 particles, whereas the top-hat filtering recognized 312 of them based on the presence of the central core. So a number of apo-ferritin cores might be present in addition to broken or incomplete proteinaceous mantles. Moreover, in this carbon calculation we did not determine the bias in our ESI-image measuring system by the application of a small particle-size carbon standard. This step is currently investigated. For that reason a comparison between the wet-chemical and *in situ* analysis is postponed.

The determined wet chemical number of iron atoms was 1,760 atoms Fe/core, a value which is different from the one which is generally assumed to be present in horse spleen ferritin (4,000-5,000 atoms/core). Reconstruction of the mean total mass of a ferritin particle based on the obtained -*in situ*- carbon atoms and the determined wet-chemical iron atoms and a P:Fe ratio of 1:9, a value of 2 kDa was calculated. This value is below the 245-440 kDa generally measured in such ferritin populations. Future investigation might elucidate the aspects of the -*in situ*- iron concentration determination.

Previously, Egerton [17, 18] has estimated in spectra the accuracy and precision of EELS quantification. Recently this has been adapted and extended for EFTEM images, including corrections for the non-linearity of the camera, shading corrections, SNR segmentation and validity checks [4]. Validity checks have been performed to evaluate the reliability of the obtained data, using a similar technique as proposed by Bonnet *et al.* [6], using STEM net-intensity images, to produce "ghost images" and to access possible specimen drift and radiation damage.

Specimen drift during the acquisition period is another factor to consider as menacing the localization sharpness, for which at least a correction step has to be available. Reduction of the total duration of the acquisition through automatic filter and spectrometer control might give some improvement in the future.

With respect to mass loss, the results collected by Hall and Gupta [22] and Lamvik *et al.* [31-34] and Zierold [58] about such losses indicate clearly that the small proteinaceous particles in or on carbon or metal films suffer from mass loss in relation to dose and specimen temperature in a rather direct way. This leads (at the same dose) to a different residual mass after an initial loss, when observed either at room temperature or at 130 K or at liquid helium temperature, where a minimal loss is noticed.

It is clear that under the conditions present in our instrument, without specimen cooling, this initial mass-loss has taken place, as the maximum beam intensity available had to be adopted to get the requested images. Although, we monitored rather modest mean losses during the additional acquisition period, the specific-element losses might be rather drastic (e.g., oxygen [16]). On the other hand, the low mean loss might be modest due to the presence of a rather firm contact between the proteinaceous material and the chromium oxide film. Metal (titanium) films have been shown to provide at ultra low liquid helium temperatures a protective factor as compared to carbon films [31-34], whereas Zierold [58] reported an improved mass-loss stability of a carbon film on frozen-hydrated sections as judged by the darkfield intensity.

There is another aspect that warns us to be careful in interpreting images that fit into a previously determined concept, according to which we see what we want to see [54]. Recent results of Bonnet and Trebbia *et al.* [5-6, 54-56] making use of a non-parametric analytical method (Multivariate statistical analysis, MSA) of the electron spectroscopic images acquired by a STEM instrument indicated that such digital images might be

considered to be composed of several components added on top of each other, like noise, shading, continuum. These components have to be analyzed and subsequently subtracted to obtain the element-related net-intensity images. Very recently, Sorber *et al.* [53] compared resultant images processed according to a parametric (power-law model) and non-parametric (MSA model) procedure using identical image sets acquired by our Zeiss 902 EFTEM. The aim was to detect any differences in the spatial distribution of the as iron-positive regarded pixels in a siderosome-containing ultrathin section. The spatial correspondence between the two models in the large siderosomal areas and in the smaller particles was rather convincing. Quantification of such images by MSA, acquired by ESI in an EM 902, has been investigated by Gelsema *et al.*, and the preliminary results look rather promising [20, 21].

In conclusion:

(1) The carbon distribution images as obtained by application of an EFTEM acquisition protocol and image-processing procedure demonstrated the proteinaceous structure of the ferritin-shell. The resultant images compared to those acquired after a negative staining procedure were significantly different, but showed minor details absent in the negatively stained ones.

(2) The proposed acquisition protocol and image-processing procedure which includes the use of calibrated attenuation filters for a variety of purposes are successfully applied. These procedures allow us to determine carbon concentration-distribution images (and presumably also of iron) in isolated ferritin particles, embedded in 2 nm thick chromium films. The reliability of these observations and calculations for structural and compositional analysis is evaluated by a number of validity checks.

(3) Mass loss, though minimal during the actual acquisition period, shows the relativity of the obtained number of 16,8 carbon atoms per ferritin shell.

This explains, that at least a certain percentage of the carbonaceous mass of the ferritin shell is preserved for measurement over the chosen acquisition period.

Acknowledgements

The skilful assistance of W.J. Visser in the production of the carbon films is gratefully acknowledged.

References

1. Andrews SB, Leapman RD (1993) Biological scanning transmission electron microscopy. Europ J Microscopy and Analysis **6**: 21-24.

2. Apkarian RP, Joy DC (1988) Analysis of metal films suitable for high-resolution SE-I microscopy. In: *Microbeam Analysis 1988* (Newbury DE, ed) San Francisco Press, San Francisco, pp 459-462.

3. Beckers ALD, Gelsema ES, de Bruijn WC (1993) An efficient method for calculating the least-squares background fit in electron energy-loss spectroscopy. J Microsc **171**: 87-92.

4. Beckers ALD, de Bruijn WC, Gelsema ES, Cleton-Soeteman MI , van Eijk HG (1994) Quantitative electron spectroscopic imaging in bio-medicine: methods for image acquisition, correction and analysis. J Microsc **174**: 171-182.

5. Bonnet N, Colliex C, Mory C, Tence M (1988) Developments in processing image sequences for elemental mapping. Scanning Microsc Suppl **2**: 351-364.

6. Bonnet N, Hannequin P (1989) Chemical mapping and multivariate statistical analysis (prospect). Ultramicroscopy **28**: 248-251.

7. Bradford MN (1976) A rapid and sensitive method for the quantitation of microgram quantities of protein utilizing the principle of protein-dye binding. Anal Biochem **72**: 245-254.

8. Colliex C, Jeanguillaume C, Mory C (1984) Unconventional modes for STEM imaging of biological structures. J Ultrastr Res **88**: 177-206.

9. Colliex C (1985) An illustrated review of various factors governing the high spatial resolution capabilities in EELS microanalysis. Ultramicrosc **18**: 131-150.

10. Colliex C, Manoubi T, Krivanek OL (1986) EELS in the electron microscope: A review of present trends. J Electron Microsc **35**: 307-313.

11. De Bruijn WC, Steijn-Myagkaya GM (1981) *In situ* X-ray microanalysis of ferritin. Beitr Elektronenmikroskop Direktabb Oberfl **14**: 423-426.

12. De Bruijn WC, Ketelaars D, Gelsema E, Sorber L (1991) Comparison of the Simplex method with several other methods for background-fitting for electron energy-loss spectral quantification. Microsc Microanal Microstruct **2**: 281-291.

13. De Bruijn WC, Sorber CWJ, Trommelen-Ketelaars GAM, Jongkind JF, Beckers ALD, Gelsema ES (1993) Electron energy-loss spectroscopy and electron probe X-ray microanalysis of biological materials: a comparative quantitative analysis of electron microscopical images. In: *X-ray microanalysis in biology: experimental techniques and applications* (Sigee DC, Morgan J, Sumner AT, Warley A, eds) Cambridge Univ Press, Cambridge, pp 81-96.

14. De Bruijn WC, Sorber CWJ, Gelsema ES, Beckers ALD, Jongkind JF (1993a) Energy-filtering transmission electron microscopy in biology. Beitr

Elektronenmikroskop Direktabb Oberfl **25**: 387-392.

15. De Bruijn WC, Sorber CWJ, Gelsema ES, Beckers ALD, Jongkind JF (1993b) Energy-filtering transmission electron microscopy of biological specimens. Scanning Microsc **7**: 693-709.

16. Drechsler M, Cantow H-J (1991) EELS data acquisition and display for the Zeiss CEM902 based on Lotus 1-2-3^{R}: application examples from a biological system and inorganic transition metal compounds. J Microsc **161**: 61-76.

17. Egerton RF (1986) *Electron Energy-Loss Spectroscopy in the Electron Microscope*. Plenum Press, New York, pp 291-352.

18. Egerton RF (1991) Factors affecting the accuracy of elemental analysis by transmission EELS. Microsc Microanal Microstruct **2**: 203-213.

19. Engel A, Reichelt R (1984) Imaging of biological structures with the scanning transmission electron microscope. J Ultrastr Res **88**: 105-120.

20. Gelsema ES, Beckers ALD, Sorber CWJ, de Bruijn WC (1992a) Correspondence analysis for quantification in electron energy-loss spectroscopy and imaging. Meth Inf Med **31**: 29-35.

21. Gelsema ES, Beckers ALD, Sorber CWJ, de Bruijn WC (1992b) Quantification procedures for electron energy-loss spectroscopy and imaging. J Microsc **166**: 287-296.

22. Hall TA, Gupta BL (1974) Beam-induced loss of organic mass under electron-microprobe conditions. J Microsc **100**: 177-188.

23. Harris DC (1978) Ion-exchange between ferritin and transferrin *in vitro*. Biochemistry **17**: 3071-3078.

24. Hayat MA (1989) In: *Principles and Techniques of Electron Microscopy*, 3rd ed, McMillan Press, London, pp 328-376.

25. Hofer F (1991) Determination of inner-shell cross-sections for EELS quantification. Microsc Microanal Microstruct **2**: 215-230.

26. Horne RW, Pasquali-Ronchetti I (1974) A negative staining-carbon film technique for studying viruses in the electron microscope. I. Preparation procedures for examining icosahedral and filamentous viruses. J Ultrastr Res **47**: 361-373.

27. Jeanguillaume C, Trebbia P, Colliex C (1978) About the use of EELS for chemical mapping of thin foils with high spatial resolution. Ultramicrosc **3**: 237-247.

28. Kleinschmidt VA, Zahn RK (1959) Über Desoxyribonucleinsäure-Molekülen in Protein Mischfilmen (DNA molecules in mixed protein films). Z Naturforsch **14b**: 770-778.

29. Körtje K-H (1994) A synthesis of energy-loss analysis and imaging. Scanning Microsc Suppl **8**.

30. Krivanek OL, Mory C, Tencé M, Colliex C (1991) EELS quantification near the single-atom detection level. Microsc Microanal Microstruct **2**: 257-267.

31. Lamvik MK, Kopf DA, Davilla SD (1987) Mass loss rate in collodion is greatly reduced at liquid helium temperature. J Microsc **148**: 211-217.

32. Lamvik MK, Davilla SD, Klatt LL (1989) Substrate properties affect the mass loss rate in collodion at liquid helium temperature. Ultramicrosc **27**: 241-250.

33. Lamvik MK, Davilla SD, Tuttle J (1989) Properties of substrates for low temperature quantitative microscopy and microanalysis. Scanning Microsc Suppl **3**, 271-276.

34. Lamvik MK, Magid AD, Davilla SD, Córdova L (1991) Temperature directly affects the rate of irradiation induced mass loss from phosphatidylcholine multilayers. Ultramicrosc **47**: 1-6.

35. Langmore JP (1978) Electron microscopy of atoms. In: *Principles and Techniques of Electron Microscopy* (MA Hayat, ed) Vol 9. Biological Applications. Van Nostrand Reinhold, New York, pp 1-63.

36. Lavergne J-L, Martin J-M, Belin M (1992) Interactive electron energy-loss elemental mapping by the "imaging spectrum" method. Microsc Microanal Microstruct **3**: 517-528.

37. Leapman RD, Hunt JA (1991) Comparison of detection limits for EELS and EDXS. Microsc Microanal Microstruct **2**: 231-244.

38. Leapman RD, Hunt JA, Buchanan RA, Andrews SB (1993) Measurements of low calcium concentrations in cryosectioned cells by parallel-EELS mapping. Ultramicrosc **49**: 225-234.

39. Leapman RD, Sun SQ, Hunt JA, Andrews SB (1993) Biological electron energy-loss spectroscopy in the field-emission STEM. Scanning Microsc Suppl **8**

40. Meyer F (1979) Iterative image transformations for an automatic screening of cervical smears. J Histochem Cytochem **27**: 128-135.

41. Ottensmeyer FP (1984) Electron spectroscopic imaging: Parallel energy filtering and microanalysis in the fixed-beam electron microscope. J Ultrastruct Res **88**: 121-134.

42. Peters K-R (1986) Rationale for the application of thin continuous metal films in high magnification electron microscopy. J Microsc **142**: 25-34.

43. Quintana C, Bonnet N (1993) Multivariate statistical analysis applied to the X-ray spectra and X-ray mapping of liver cell nuclei. Scanning Microsc Suppl **8**

44. Reimer L (1991) Energy filtering transmission electron microscopy. In: *Advances in Electronics and Electron Physics* Vol **81**, Academic Press, London, New York, pp 43-126.

45. Ringeling PL (1991) Rat liver ferritin biochemical and microanalytical aspects. Doctoral Thesis, Erasmus University, Rotterdam, The Netherlands.

46. Ringeling PL, Cleton MI, Kroos MJ, Sorber CWJ, de Bruijn WC, Harrison PM (1989) Lysosomal and cytosolic ferritins. A biochemical and electron-spectroscopic study. Biol Metals **2**: 114-121.

47. Ringeling PL, Cleton MI, Huijskes-Heins MIE, Seip MJE, de Bruijn WC, van Eijk HG (1990) Analysis of iron-containing compounds in different compartments of the rat liver after iron loading. Biol Metals **3**: 176-182.

48. Shuman H, Somlyo AP (1987) Electron energy-loss analysis of near-trace-element concentrations of calcium. Ultramicrosc **21**: 23-32.

49. Sorber CWJ, de Jong AAW, den Breejen NJ, de Bruijn WC (1991a) Quantitative energy-filtered image analysis in cytochemistry. I. Morphometric analysis of contrast-related images. Ultramicrosc **32**: 55-68.

50. Sorber CWJ, van Dort J-B, Ringeling PC, Cleton-Soeteman MI, de Bruijn WC (1991b) Quantitative energy-filtered image analysis in cytochemistry. II. Morphometric analysis of element-distribution images. Ultramicrosc **32**: 69-79.

51. Sorber CWJ, Ketelaars GAM, Gelsema ES, Jongkind JF, de Bruijn WC (1992a) Quantitative analysis of electron energy-loss spectra from ultrathin-sectioned biological material. I. Optimization of the background fit with the use of Bio-standards. J Microsc **162**: 23-42.

52. Sorber CWJ, Ketelaars GAM, Gelsema ES, Jongkind JF, de Bruijn WC (1992b) Quantitative analysis of electron energy-loss spectra from ultrathin-sectioned biological material. II. The application of Bio-standards for quantitative analysis. J Microsc **162**: 43-53.

53. Sorber L, Bonnet N, Gelsema E, Jongkind H, Beckers G, de Bruijn W (1992) Multivariate statistical analysis as a tool for the analysis of EELS-images. Beitr Elektronenmikroskop Direktabb Oberfl **25**: 393-398.

54. Trebbia P, Manoubi T (1989) From experiments to interpretation: Confidence limits. Ultramicrosc **28**: 266-276.

55. Trebbia P, Bonnet N (1990) EELS elemental mapping with unconventional methods. I. Theoretical basis: image analysis with multivariate statistics and entropy concepts. Ultramicrosc **34**: 165-178.

56. Trebbia P, Mory C (1990) EELS elemental mapping with unconventional methods. II. Applications to biological specimens. Ultramicrosc **34**: 179-203.

57. van Gelder W, Siersema PD, Voogd A, de Jeu-Jaspars NCM, van Eijk HG, Koster JF, de Rooy FWM, Wilson JHP (1993) The effect of desferrioxamine on iron metabolism and lipid peroxidation in hepatocytes of C57BL/10 mice in experimental uroporphyria. Biochem Pharmacol **46**: 221-228.

58. Zierold K (1988) X-ray microanalysis of freeze-dried and frozen-hydrated crysections. J Electr Microsc Techn **9**: 65-82.

Discussion with Reviewers

R. Leapman and K.-H. Körtje: What was the approximate electron dose required to obtain the ferritin images?

Authors: We refrained from giving an exact figure for the electron dose. We used the maximum intensity from the hair-pin source. Ignoring the time for object selection and focusing, the number of images taken in one acquisition sequence is minimally fifteen (five before, three beyond, three zero-loss, four for the correction procedures). The integration time per image is 256x40 ms, the time required to adopt the spectrometer/filter settings and image transfer is about 1 min. per step, so the dose is enormous.

K.-H. Körtje: Can the authors give more information about the validity checks?

Authors: The nature of the validity checks is described elsewhere [4]; briefly, the main instabilities are the beam and specimen drift during the acquisition of the image sequences. A correction program compensates any deviation of the pixel alignment along the image sequence, when this turns-out to happen. A more serious problem is the electron-beam instability. Slight lateral variations influence the shading correction procedure, so that a residual shading remains present in one of the corners (which was the case in Figure 7). The reason to use the central part of the final processed image as we did here, included the aspect to eliminate also the effects of such an instability on the quantitative results. The formation of ghost images to monitor the absence of any residual non-element related intensities is as follows. Off-line, four pre-edge carbon images are mathematically processed to calculate the continuum image of the fifth carbon pre-edge image. When the fitting and correction procedures are correctly applied there are no residual intensities between the actual fifth image and that estimated ghost image. In addition, the program tests for compliance with $t/\lambda < 1$, parameters related to section thickness (t) and mean free path (λ). The mass-loss determination will be described below.

R. Leapman: Can you give some potential biological applications of carbon imaging in the EFTEM?

Authors: Our principle aim was to use the ferritin particles as an object for the quantitative measurements

for iron and carbon, in which the iron concentration determination was adjourned due to the large interference of the two edges and that of the carbon remained. In our opinion, the most important aim for carbon imaging of isolated particles on thin non-carbonaceous substrates is the fact that the architecture is not disturbed by the negative stain distribution, and the possibility to use any positive stain in combination with the carbon imaging for intramolecular structural discrimination.

K.-H. Körtje: Is it possible to quantify the mass loss during image acquisition of the ferritin lakes on the chromium film?
Authors: In the literature, arguments are given that mass loss might be considered to be a time/specimen-temperature related event, in which mass loss after an initial uncontrolled negative exponential loss is stabilized around a residual constant mass, the level of which is related to the (cooled/uncooled) specimen temperature [31-34]. We did our experiments during that rather constant-loss phase. One of the validity checks is the retake of the first image at the end of the series. The mean grey-value change between the first and the last retake of the first image was virtually negligible.